## Journal of Materials Chemistry A



## **PAPER**

View Article Online
View Journal | View Issue



Cite this: J. Mater. Chem. A, 2020, 8, 25306

Received 21st August 2020 Accepted 13th November 2020

DOI: 10.1039/d0ta08238d

rsc.li/materials-a

# Doping by design: finding new n-type dopable ABX<sub>4</sub> Zintl phases for thermoelectrics†

Jiaxing Qu, Da Vladan Stevanović, Elif Ertekin Da and Prashun Gorai D\*b

Doping remains a bottleneck in discovering novel functional materials for applications such as thermoelectrics (TE) and photovoltaics. The current computational approach to materials discovery is to identify candidates by predicting the functional properties of a pool of known materials, and hope that the candidates can be appropriately doped. What if we could "design" new materials that have the desired functionalities and doping properties? In this work, we use an approach, wherein we perform chemical replacements in a prototype structure, to realize doping by design. We hypothesize that the doping characteristics and functional performance of the prototype structure are translated to the new compounds created by chemical replacements. Discovery of new n-type Zintl phases is desirable for TE; however, n-type Zintl phases are a rarity. We demonstrate our doping design strategy by discovering 7 new, previously-unreported ABX<sub>4</sub> Zintl phases that adopt the prototypical KGaSb<sub>4</sub> structure. Among the new phases, we computationally confirm that NaAlSb<sub>4</sub>, NaGaSb<sub>4</sub> and CsInSb<sub>4</sub> are n-type dopable and potentially exhibit high n-type TE performance, even exceeding that of KGaSb<sub>4</sub>. Our structure prototyping approach offers a promising route to discovering new materials with designed doping and functional properties.

## 1 Introduction

Doping has been an enduring and pervasive challenge in the discovery of new functional materials for thermoelectrics,1,2 transparent conductors, 3,4 photovoltaics, 5,6 etc. There are several challenges in doping materials: (1) cannot be sufficiently doped with either electrons (n-type) or holes (p-type) i.e., the material is an insulator, or (2) cannot be doped with the desired carrier type (doping asymmetry), or (3) cannot be doped to the desired carrier concentration needed for the specific application. For instance, wide band gap oxides such as SiO2 and Al2O3 are insulators that cannot be doped either n- or p-type. Some materials suffer from doping asymmetry, wurtzite ZnO being one of the prominent examples. While n-type doping of ZnO is achieved by Al doping, p-type doping remains elusive.7 Doping asymmetry has practical implications. ZnSb is predicted to be a promising n-type TE material;8 however, it has been shown theoretically9 and experimentally10 that n-type doping cannot be achieved. The low formation energy of acceptor Zn vacancies lead to degenerate p-type doping behavior of ZnSb.9

Within intermetallic compounds, there exists a subset known as Zintl phases that generally exhibit doping asymmetry. To date, most well-known Zintl phases with moderate carrier concentrations are native p-type due to self-doping. However, only a few n-type ones have been reported in experiments.<sup>11-14</sup> The inherent features of Zintl phases, such as small band gaps, dispersive electronic bands, and complex structures, make them suitable as TE materials. Zintl phases such as Yb<sub>14</sub>-MnSb<sub>11</sub>,<sup>15</sup> CaZn<sub>2</sub>Sb<sub>2</sub> (ref. 16) and Ca<sub>5</sub>Al<sub>2</sub>Sb<sub>6</sub> (ref. 17) are among the TE materials with the best performance in the mid- to high-temperature regime. The experimental data in Fig. 1 demonstrate the well-known doping asymmetry in Zintl phases. The maximum electronegativity difference is a measure of the bonding ionicity between the cation–anion framework. The p-type Zintl phases, denoted by blue markers, outnumber the n-type phases (red markers).

Computational predictions indicate that Zintl phases when doped n-type have comparable or better TE performance than their p-type versions. However, the discovery of new n-type Zintl phases so far has been driven by chemical intuition and serendipity. The recent discoveries of new n-type Zintl phases, including KAlSb<sub>4</sub>, KGaSb<sub>4</sub>, RGaSb<sub>4</sub>, CSGaSb<sub>4</sub>, and Ba<sub>3</sub>Cd<sub>2</sub>P<sub>4</sub>, seem to suggest that (1) there are Zintl phases that may overcome doping asymmetry, and (2) the chemical and structural phase space of n-type Zintl phases is largely underexplored. One plausible route for finding new n-type dopable Zintl phases with high TE performance is by chemical replacements in the structure prototype (CRISP). Computational efforts in the past have utilized chemical substitution in known compounds to search for undiscovered phases. Color in the last decade, various routes have been explored to search for as-yet-

<sup>&</sup>lt;sup>a</sup>University of Illinois at Urbana-Champaign, Urbana, IL 61801, USA <sup>b</sup>Colorado School of Mines, Golden, CO 80401, USA. E-mail: pgorai@mines.edu † Electronic supplementary information (ESI) available. See DO 10.1039/d0ta08238d

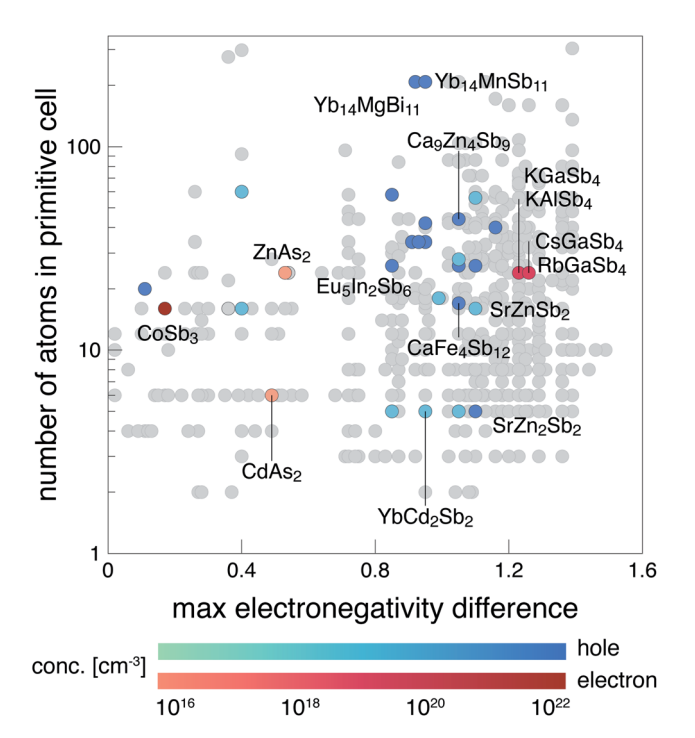


Fig. 1 Binary and ternary Zintl phases from the ICSD represented by the number of atoms in the primitive cell and the maximum electronegativity difference (on the Pauling scale) between the constituent elements. The color scheme denotes the experimentally measured charge carrier concentrations of 46 Zintl phases, with blue denoting the p-type (hole) and red n-type (electron). KGaSb<sub>4</sub> and CoSb<sub>3</sub> can be doped both n- and p-type; only n-type is shown for clarity. n-Type Ba<sub>3</sub>Cd<sub>2</sub>P<sub>4</sub> is not shown because the carrier concentration has not been measured yet.<sup>14</sup> Data adapted from ref. 18, with permission from the Royal Society of Chemistry

unknown materials for functional applications. 22-25 These studies served the general purpose of discovering new compounds rather than new compounds with designed functionalities.

In this work, we show that chemical substitutions in appropriately chosen prototype structures is a viable route to discovering new compounds with designed doping properties. Chemical substitutions (or replacements) in the prototype structure generates iso-structural compounds that are ordered, with each site fully occupied by an element, which is in contrast to disordered alloys with partially-occupied atomic sites. Selecting an appropriate prototype structure is one of the key aspects of this approach. The prototype should possess the same functionality (e.g. high TE performance) and doping (e.g. n-type dopable) characteristics that we desire to "transfer" to the new compounds created by chemical substitutions. We demonstrate this approach to discover new ABX<sub>4</sub> Zintl phases (A = Na, K, Rb, Cs; B = Al, Ga, In; X = As, Sb, Bi) that adopt the KGaSb<sub>4</sub> prototype structure (Fig. 2), predicted to have high TE performance and are n-type dopable. KGaSb4 serves as an appropriate prototype for two reasons: (1) it has good n-type TE performance, with  $zT \sim 1$ , and (2) can be doped n-type to >10<sup>19</sup> cm<sup>-3</sup> electron concentrations. Out of the 36 plausible Zintl phases, only 2 are reported in the Inorganic Crystal Structure

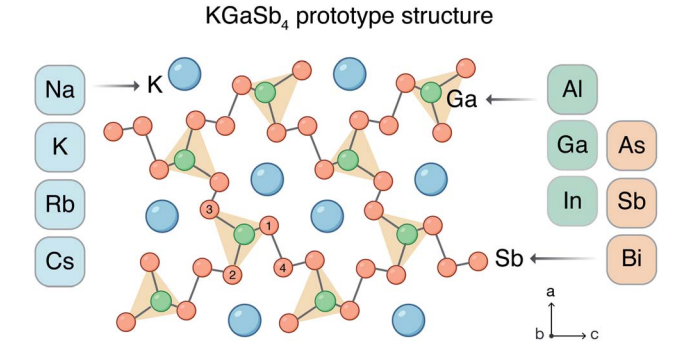


Fig. 2 Crystal structure of KGaSb<sub>4</sub>, a Zintl phase with an anionic framework composed of [GaSb<sub>4</sub>] tetrahedra linked by homoatomic Sb-Sb bonds. K atoms occupy the channels formed by the anionic framework. We perform chemical replacements in the prototypical KGaSb<sub>4</sub> structure, where K is replaced with Na, K, Rb, and Cs, Ga with Al, Ga, and In, and Sb with As, Sb, and Bi. Sb has four unique Wyckoff sites, labelled 1 through 4.

Database (ICSD)26 and four of them have been recently discovered,13 indicating that the phase space of KGaSb4 type Zintl phases is under-explored. Importantly, the 6 known ABX<sub>4</sub> phases are all n-type dopable. 12,13 Using first-principles calculations, we theoretically evaluate the thermodynamic and dynamic stability of the 36 ABX<sub>4</sub> Zintl phases and predict that 13 of them should be stable, including the 6 known phases (KGaSb<sub>4</sub>, KAlSb<sub>4</sub>, CsGaSb<sub>4</sub>, CsAlSb<sub>4</sub>, RbGaSb<sub>4</sub>, and RbAlSb<sub>4</sub>) and 7 new phases. Of the 7 undiscovered phases, we choose the top 3 candidates (NaAlSb<sub>4</sub>, NaGaSb<sub>4</sub> and CsInSb<sub>4</sub>) that are predicted to have the highest n-type TE performance; first-principles defect calculations reveal that they are all n-type dopable.

#### 2 Methods

The computational workflow is summarized in Fig. 3. We create hypothetical Zintl phases by chemical replacements in the prototype KGaSb<sub>4</sub> structure and relax them with DFT. Next, we calculate their electronic structures and theoretical TE performance. Subsequently, we assess the thermodynamic and dynamic stability of these structures with predicted high n-type TE performance. Finally, we assess the n-type dopability of the top candidates using first-principles defect calculations.

## 2.1 Chemical replacements in the prototype structure

Chemical substitutions are performed in the prototype structure KGaSb4 to create hypothetical ABX4 compounds. With consideration to nominal oxidation states and electronegativity, we choose alkali elements Na, K, Cs, and Rb for the A site, group 13 elements (Al, Ga, and In) for the B site, and pnictides (As, Sb, and Bi) for the X site. The orthorhombic crystal structure of KGaSb<sub>4</sub> (Pnma) consists of an anionic framework formed by three subunits that extend infinitely along the b axis: cornersharing [GaSb<sub>4</sub>] tetrahedra, Sb-Sb zigzag chains and Sb-Sb trigonal pyramidal chains. The herringbone-like Ga-Sb networks form channels in the a-c plane, with the K atoms occupying these channels (Fig. 2). The small electronegativity

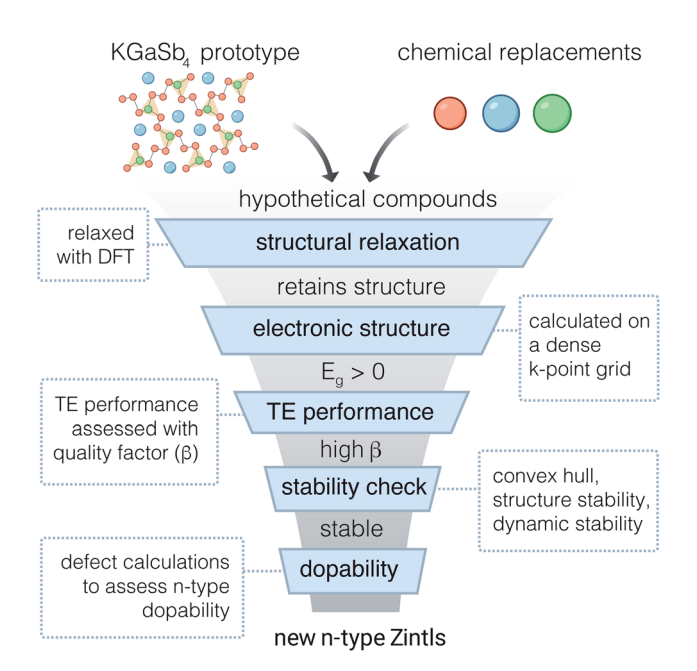


Fig. 3 Schematic computational workflow of chemical replacements in the structure prototype approach. Here,  $E_{\rm g}$  is the band gap and  $\beta$  is the predicted thermoelectric quality factor, a measure of thermoelectric performance. Specifically, n-type  $\beta$  is considered.

difference between Ga and Sb ( $\Delta\chi_{\text{Ga-Sb}} = 0.24$  on the Pauling scale) gives rise to the covalent nature of the anionic frameworks, while the high electropositivity of K ( $\Delta\chi_{\text{K-Sb}} = 1.23$ ) leads to ionic bonding with the anionic frameworks *i.e.*, electron transfer from K to the anionic framework.

## 2.2 Structure relaxation and the electronic structure

The hypothetical structures generated using chemical substitutions are relaxed with density functional theory (DFT) using the plane-wave VASP code.27 The Perdew-Burke-Ernzerhof (PBE) exchange correlation functional28 is used within the generalized gradient approximation (GGA). The core and valence electrons are treated with the projector-augmented wave (PAW) method.29 The hypothetical structures are relaxed with a plane-wave energy cutoff of 340 eV and a Monkhorst-Pack k-point sampling. The space groups of the relaxed structures are then determined to check whether they retain the prototype structure. Electronic structures are calculated on dense k-mesh with a fixed number of k-points. The k-point grid is determined according to the equation:  $N_{\text{atoms}} \times N_{\text{kpts}} \simeq 8000$ , where  $N_{\text{atoms}}$  is the number of atoms in the primitive cell and  $N_{
m kpts}$  is the number of k points. Structures with zero DFTcalculated band gaps are not considered in the subsequent steps. Therefore, hypothetical compounds that retain the prototype structure and have non-zero band gaps are considered for further analysis.

## 2.3 Thermoelectric performance assessment

The quality factor  $(\beta)$  provides a measure of the potential for thermoelectric performance of a material. We have previously

developed semi-empirical models to computationally evaluate  $\beta$  (see ref. 30 for details). The quality factor is expressed in terms of the electronic and lattice thermal transport parameters as:

$$\beta \propto \frac{\mu_0 m_{\rm DOS}^*^{3/2}}{\kappa_{\rm L}} T^{5/2}$$
 (1)

where  $\mu_0$  is the intrinsic charge carrier mobility at 300 K,  $m_{DOS}^*$  is the density-of-states (DOS) effective mass, and  $\kappa_L$  is the lattice thermal conductivity at 300 K. Semi-empirical models of  $\mu_0$  and  $\kappa_{\rm L}$  allow computational assessment of the quality factor<sup>30,31</sup> with first-principles calculations. To determine  $\mu_0$  and  $\kappa_L$  from the semi-empirical models, band degeneracy (Nb), DOS effective mass  $(m_{\text{DOS}}^*)$  and bulk modulus (B) need to be determined.  $m_{\text{DOS}}^*$ is determined from the DOS within the single parabolic band approximation, such that the parabolic band reproduces the same number of states as the DOS within a 100 meV energy window from the relevant band edges. With  $m_{DOS}^*$  and  $N_b$ , the band effective mass  $(m_b^*)$  can be determined within the parabolic and isotropic band approximation:  $m_{\rm b}^* = m_{\rm DOS}^* N_{\rm b}^{-2/3}$ . The bulk modulus B is obtained by fitting the Birch-Murnaghan equation of state.<sup>32</sup>  $\kappa_L$  is calculated using a semi-empirical model based on the modified Debye-Callaway model;31 the model inputs are the bulk modulus (B), density, volume per atom, average atomic mass, average coordination number, and the number of atoms in the primitive cell. Besides B, the other model parameters are directly accessible from the structure.

We have previously demonstrated that the computed  $\beta$  correctly predicts the experimentally observed performance of well-known TE materials such as PbTe ( $\beta_n$ ,  $\beta_p \sim 15$ ), PbSe, PbS, CoSb<sub>3</sub>, SnSe, and Mg<sub>3</sub>Sb<sub>2</sub>.30,33 Moreover, the differences in nand p-type  $\beta$  values also correctly capture the experimental trends. For example,  $\beta_n$  of Mg<sub>3</sub>Sb<sub>2</sub> (~19) is significantly larger than  $\beta_p$  (~2), which is consistent with the high n-type TE performance. The higher  $\beta_{\rm p} \sim 23$  of the *Cmcm* phase of SnSe compared to  $\beta_n \sim 3$  is also consistent with experimentally realized TE performance.33 In fact, we have previously shown that the high  $\beta_n$  of the titular compounds *i.e.*, ABX<sub>4</sub> Zintl phases, can be realized in experiments. 11 KGaSb<sub>4</sub> ( $eta_{
m n}\sim 15$ ) exhibits  $zT\sim$ 1 even without rigorous optimization.12 Given the excellent agreement between predictions based on  $\beta$  and experiments, we believe that  $\beta$  can be used to reliably predict the TE performance of new materials.

## 2.4 Stability assessment

Compositional stability. Stability against chemical decomposition into competing phases can be assessed with convex hull analysis. The energies of ABX $_4$  compositions as well as different binary and ternary competing phases are calculated. Materials on the convex hull are stable. The energy above the convex hull ( $\Delta E_{\rm hull}$ ) is an indicator of the compositional stability of the ABX $_4$  phase. If the ABX $_4$  phase lies on the hull or within 20 meV per atom from the hull, it is deemed to be compositionally stable. The compounds that lie within 20 meV per atom of the convex hull could be deemed compositionally stable due to the typical DFT prediction errors. The competing phases are searched within the ICSD. The total energies of the competing

phases are calculated by relaxing the structures with the same methodology as described in Section 2.2. The formation enthalpies are calculated from the total energies and reference chemical potentials of the elemental phases. The reference chemical potentials are obtained by fitting to a set of experimentally measured formation enthalpies, similar to the procedure described in ref. 37, which has been shown to provide accurate predictions for formation enthalpies. See the ESI† for the fitted reference chemical potentials.

Structural stability. The aim of the structural stability analysis is to find if the lowest-energy (most favorable) structure for a given ABX4 composition is the prototype structure. Plausible structures are selected from the ICSD<sup>26</sup> that can accommodate 1-1-4 ternary stoichiometries. In order to identify plausible 1-1-4 stoichiometry structures, we impose further the following constraints: cations on A and B sites with compatible oxidation states (1+ for A, and 3+ for B). To assess structural stability, each ABX<sub>4</sub> composition is fully relaxed in all plausible structures chosen from the ICSD, including in the prototype KGaSb<sub>4</sub> structure. Structure relaxation is performed as described in Section 2.2. The most favorable structure is the lowest-energy structure; if the prototype KGaSb<sub>4</sub> structure is the lowest-energy structure, then the ABX<sub>4</sub> composition is deemed structurally stable.

Dynamic stability. For ABX<sub>4</sub> Zintl phases that are found to be compositionally and structurally stable, we test their dynamic stability w.r.t.  $\Gamma$ -point phonons using density functional perturbation theory (DFPT), as implemented in VASP.27 The structures are relaxed with a plane-wave energy cutoff of 520 eV with an energy convergence criterion of 10<sup>-8</sup> eV. The Brillouin zone is sampled using a  $\Gamma$ -centered 4  $\times$  4  $\times$  2 Monkhorst–Pack k-point grid. Structures with no imaginary frequencies at the  $\Gamma$ point are considered dynamically stable. We also calculate the full phonon dispersion for three stable ABX4 phases using the supercell finite-displacement method implemented in the Phonopy package, 38,39 with VASP as the force calculator. The self-consistent calculations in VASP are performed with the same plane-wave energy cutoff and k-point grid as the DFPT calculations, with an energy convergence criterion of  $10^{-8}$  eV.

#### Defect energetics 2.5

To understand the defect chemistry of ABX4 Zintl phases, we employ the standard supercell approach to calculate the defect formation energies of native point defects. The defect formation energy  $(\Delta E_{\mathrm{D},q})$  is calculated from the total energies as follows:

$$\Delta E_{\mathrm{D},q} = E_{\mathrm{D},q} - E_{\mathrm{host}} + \sum_{i} n_i \mu_i + q E_{\mathrm{F}} + E_{\mathrm{corr}}$$
 (2)

where  $\Delta E_{\mathrm{D},q}$  represents the formation energy of a defect D in charge state q;  $E_{D,q}$  and  $E_{host}$  are the total energies of the supercell with and without the defects, respectively,  $E_{\rm F}$  is the Fermi energy which varies from the valence band maximum (VBM) to the conduction band minimum (CBM),  $E_{corr}$  is the term that accounts for the finite-size corrections within the supercell approach,  $\mu_i$  is the chemical potential of elemental species i added  $(n_i < 0)$  or removed  $(n_i > 0)$  from the host

supercell to form defects. The elemental chemical potential  $\mu_i$  is expressed as  $\mu_i = \mu_i^0 + \Delta \mu_i$ , where  $\mu_i^0$  is the reference elemental potential (see Section 2.4) and  $\Delta \mu_i$  is the deviation from the reference elemental phase. The bounds on  $\Delta \mu_i$  are set by the thermodynamic stability conditions, with  $\Delta \mu_i = 0$  corresponding to i-rich conditions and a large negative value of  $\Delta \mu_i$ represents i-poor growth conditions.

First-principles defect calculations are performed using the GGA-PBE exchange correlation functional. The Brillouin zone of the 192-atom supercells is sampled using a  $\Gamma$ -centered 2  $\times$  2  $\times$  2 k-grid. The atomic positions in the defect supercells are fully relaxed to obtain the total energies. The following corrections to the defect formation energies are included in  $E_{corr}$  as described in ref. 40: (1) image charge correction for charged defects, (2) potential alignment correction for charged defects, (3) bandfilling corrections for shallow defects, and (4) band gap correction. The static dielectric constant (electronic + ionic), which is needed for calculating the image charge correction, is evaluated using DFPT. To correct the band gap under-estimation in GGA-PBE, we employ state-of-the-art GW quasiparticle energy calculations to compute the band edge shifts relative to the DFT band edge positions.41 A computational framework for automation of point defect calculations, pylada-defects, 42 is utilized in this work for creating the defect supercells and analysis of the results, including calculations of finite-size corrections.

The formation energies for the native point defects (vacancy, anti-site defect, and interstitial) are calculated in charge states q =-3, -2, -1, 0, +1, +2, and +3. All unique Wyckoff positions in the crystal structures (Fig. 2) are considered in the calculations for vacancies and anti-site defects. The likely interstitial sites are determined by a Voronoi tessellation scheme, as implemented in pylada-defects.42 In each structure, we consider up to 20-25 possible interstitial sites and then determine the lowest-energy site based on the total energies of the relaxed supercells. The free carrier concentrations at specific temperatures are calculated self-consistently by solving the charge-neutrality conditions.

#### 3 Results and discussion

Fig. 4(a) presents the summary of the computational search of new ABX<sub>4</sub> Zintl phases in the prototypical KGaSb<sub>4</sub> structure. Out of the 36 phases considered in this study, only 6 are known/ reported,11-13 indicating that the chemical phase space of the ABX<sub>4</sub> compound is under-explored. From electronic structure calculations, we find that 25 out of the 36 ABX4 phases (in the assumed KGaSb4 structure) have a non-zero DFT band gap (Fig. 4(a)). Furthermore, 22 out of 25 have n-type  $\beta$  larger than that of PbTe, a well-known thermoelectric material. Of the remaining 22 compositions, we find that 13 of them are stable compositionally (within 20 meV per atom from the convex hull), structurally (most favorable in the KGaSb<sub>4</sub> structure), and dynamically (no imaginary phonon frequencies).

## 3.1 Stability assessment

Our stability analysis reveals 13 stable ABX4 phases that are either on or within 20 meV per atom from the convex hull (Table

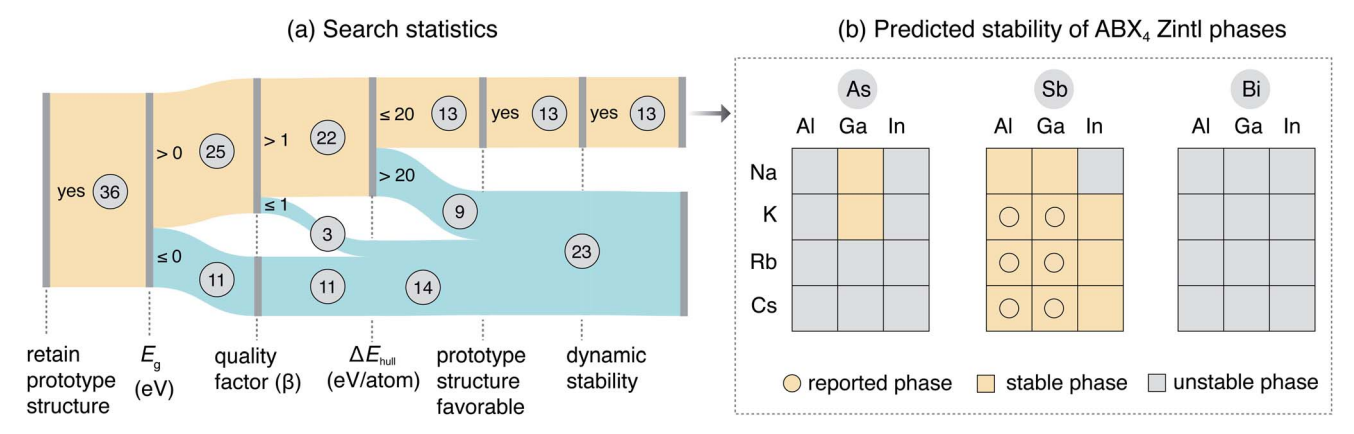


Fig. 4 Statistics of the search for new ABX<sub>4</sub> Zintl phases: (a) Sankey plot of the material screening, resulting in the identification of 13 stable phases, including the 6 known and 7 newly predicted phases. (b) Chemical search space of 36 ABX4 Zintl phases, with known phases (from the ICSD or reported in ref. 13) denoted by circles. Yellow and grey boxes correspond to stable and unstable phases from our stability predictions,

1), most stable in the KGaSb<sub>4</sub> prototype structure, and dynamically stable w.r.t.  $\Gamma$ -point phonon modes. These 13 phases include the 6 known/reported phases (KAlSb<sub>4</sub>, 11 KGaSb<sub>4</sub>, 12 CsAlSb<sub>4</sub>, 13 CsGaSb<sub>4</sub>, 13 RbAlSb<sub>4</sub>, 13 and RbGaSb<sub>4</sub>, 13) and 7 as-yetunknown phases (NaAlSb4, NaGaAs4, KGaAs4, NaGaSb4, KInSb<sub>4</sub>, RbInSb<sub>4</sub>, and CsInSb<sub>4</sub>). Through our stability assessment, we correctly predict the existence of the 6 known experimentally synthesized phases, which lends credence to our stability predictions. Among the 13 stable phases, 8 of them lie on the hull while the remaining 5 are above the hull but within 20 meV per atom (Table 1). These predicted stable compounds comprise 2 arsenides and 11 antimonides. We find that all the bismuthides are thermodynamically unstable, which is consistent with synthesis attempts in ref. 13. Our convex hull analysis shows that the primary competing phases, which restrict the compositional stability of the ABX<sub>4</sub> phases, are ternary A<sub>2</sub>B<sub>2</sub>X<sub>3</sub> phases. For instance, Na<sub>2</sub>Al<sub>2</sub>Sb<sub>3</sub> and NaSb compete with NaAlSb<sub>4</sub> under the most Na-rich growth conditions.

For establishing structural stability, we consider 34 plausible structures from the ICSD<sup>26</sup> using the criteria explained in the Methods (Section 2.4). The full list of the 34 structures are provided in the ESI.† We perform structural stability analysis on all 13 compositionally stable phases and find that all of them are structurally stable in the prototype KGaSb<sub>4</sub> structure. Furthermore, we find that all 13 phases are dynamically stable at the  $\Gamma$ -point (see the ESI†).

To further confirm the dynamic stability, we calculated the full-path phonon dispersions of the 3 newly predicted phases -NaAlSb<sub>4</sub>, NaGaSb<sub>4</sub> and CsInSb<sub>4</sub> (see in Fig. 5). See Section 3.3 for the reasons why we chose these three candidate materials. The absence of imaginary phonon modes in the phonon bandstructure further confirms the dynamic stability of NaAlSb4, NaGaSb<sub>4</sub> and CsInSb<sub>4</sub>. As expected, the low-energy modes are dominated by contributions from the heavy element Sb. The phonon dispersions (Fig. 5) feature low-energy optical modes (<1 THz) that appear to hybridize with the acoustic modes. It

Table 1 Computed electronic structure parameters, transport properties, and thermoelectric performance of 13 ABX<sub>4</sub> Zintl phases that are predicted to be stable in the KGaSb<sub>4</sub> structure.  $\beta$  (n-type) is referenced to n-type  $\beta$  of PbTe (15),  $N_{b,CB}$  is the conduction band degeneracy,  $\kappa_L$  is the room-temperature lattice thermal conductivity,  $\mu_0$  is the room-temperature electron mobility and  $\Delta E_{\text{hull}}$  is the energy above the convex hull. \* denotes the known ABX<sub>4</sub> phases

Phases	$eta/eta_{ ext{PbTe}}$ (n-type)	$N_{ m b,CB}$	$\kappa_{\rm L}  ({ m W} \; { m m}^{-1} \; { m K}^{-1})$	$\mu_{\rm n}  ({\rm cm^2  V^{-1}  s^{-1}})$	$\Delta E_{\text{hull}}$ (meV per atom)
	( 71 )	5,65	2 ( )	, (	
NaGaSb <sub>4</sub>	4.8	7	1.0	88	7
NaAlSb <sub>4</sub>	4.5	6	1.0	124	17
CsInSb <sub>4</sub>	1.7	2	1.2	136	0
CsGaSb₄*	1.7	2	0.9	117	0
RbInSb <sub>4</sub>	1.6	2	1.2	141	0
KInSb <sub>4</sub>	1.6	2	1.3	150	4
CsAlSb <sub>4</sub> *	1.5	2	0.9	98	0
RbGaSb <sub>4</sub> *	1.5	2	0.9	105	0
KGaSb <sub>4</sub>	1.5	2	1.0	106	0
$RbAlSb_4^*$	1.4	2	1.0	88	0
KGaAs <sub>4</sub>	1.4	2	1.4	123	12
KAlSb <sub>4</sub>	1.3	2	1.0	93	0
NaGaAs <sub>4</sub>	1.2	2	1.4	93	19

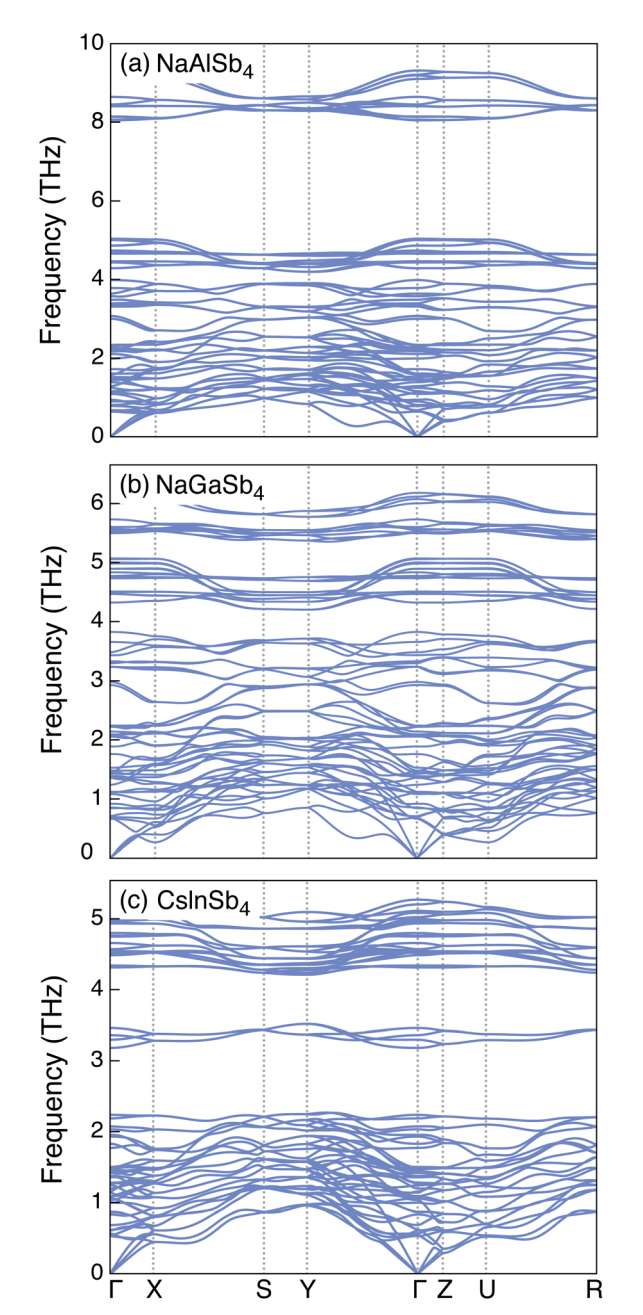


Fig. 5 Phonon dispersions of (a) NaAlSb<sub>4</sub>, (b) NaGaSb<sub>4</sub> and (c) CslnSb<sub>4</sub> along the special k-point paths of the Brillouin zone of an orthorhombic lattice.

has been shown that such acoustic-optical hybridization can lead to increased scattering of the primary heat-carrier acoustic modes, resulting in low lattice thermal conductivities. 43

## Electronic structure of ABX<sub>4</sub> phases

Fig. 6 presents the electronic band structures of NaAlSb<sub>4</sub>, NaGaSb<sub>4</sub>, and CsInSb<sub>4</sub>. The band structures are plotted along the special k-point paths of the orthorhombic Brillouin zone. The band gap underestimation in DFT is adjusted by applying band edge shifts calculated with GW quasi-particle energy calculations (see Section 2.5). NaAlSb<sub>4</sub>, NaGaSb<sub>4</sub>, and CsInSb<sub>4</sub>

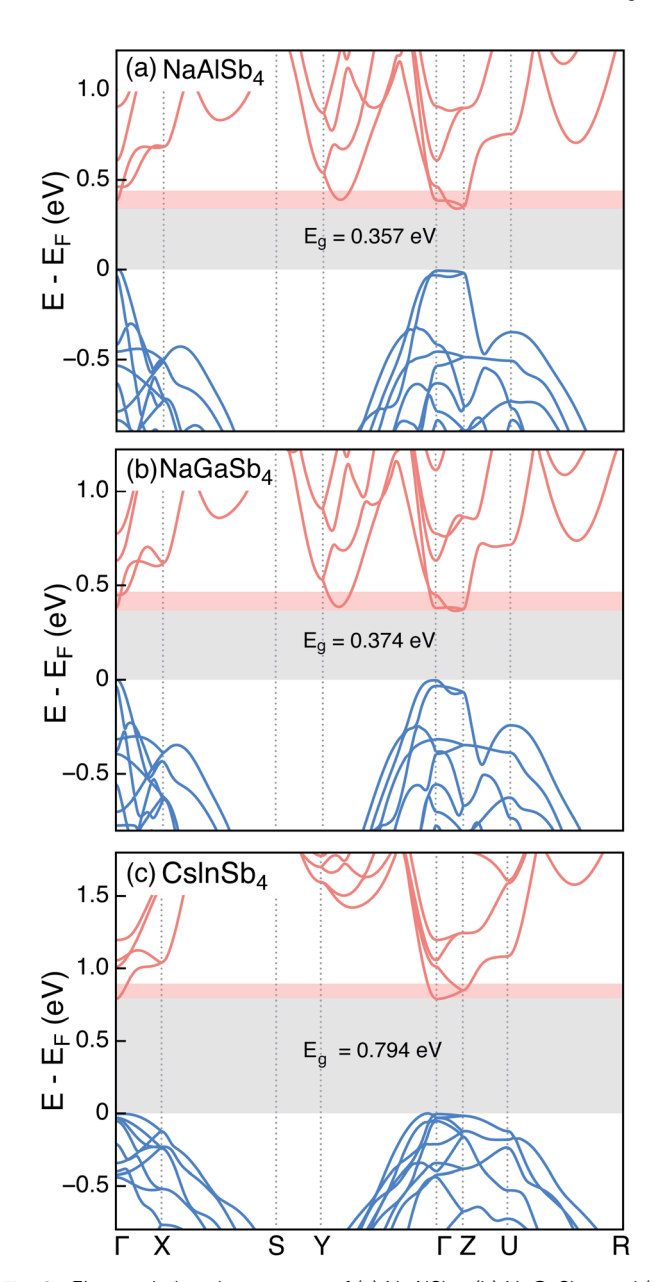


Fig. 6 Electronic band structures of (a) NaAlSb<sub>4</sub>, (b) NaGaSb<sub>4</sub>, and (c)  $CsInSb_4$  along the special k-point paths of the Brillouin zone of an orthorhombic lattice. The grey shaded region shows the band gap and red shaded region indicates the 100 meV energy window used for fitting  $m_{\text{DOS,CB}}^*$  and extracting  $N_{\text{b,CB}}$ . Note that the band edge positions are obtained from GW quasi-particle energy calculations

are all small band gap semiconductors (<1 eV), which is typical of Zintl phases. CsInSb4 has a larger band gap compared to NaAlSb<sub>4</sub> and NaGaSb<sub>4</sub> owing to the larger electronegativity difference between Cs and In. In all three phases, there exists conduction band (CB) valleys at  $\Gamma$  and at Z. In NaAlSb<sub>4</sub> and NaGaSb<sub>4</sub>, there are additional CB valleys along  $\Gamma$ - $Y(N_b = 2)$  and  $\Gamma$ -Z ( $N_{\rm b}=2$ ) that also lie within the 100 meV energy window from the CBM shown by the red shaded region in Fig. 6. In NaAlSb<sub>4</sub> and NaGaSb<sub>4</sub>, the CBM lies along  $\Gamma$ -Z while in CsInSb<sub>4</sub>, the CBM is located at  $\Gamma$ . The electronic structure of other ABX<sub>4</sub> phases is available in the ESI.† We also calculated the electronic

0.2-0.3 > 0.3

1.4

structure of CsInSb<sub>4</sub> with relativisitic spin-orbit coupling (SOC) included (at the DFT level of theory), which is shown in Fig. S2 in the ESI.† We find that while the band gap decreases from 0.79 eV (Fig. 6(c)) to 0.63 eV (Fig. S2†), the features of the conduction band (e.g., effective mass) and therefore, the predicted n-type TE performance remain unchanged with the inclusion of SOC.

When band valleys (or pockets) do not lie at special k-points, it increases band degeneracy due to symmetry. Consequently, NaAlSb<sub>4</sub> and NaGaSb<sub>4</sub> have high conduction band degeneracies of 6 and 7, respectively. High band degeneracy coupled with low band effective mass enhances charge transport properties for thermoelectrics, including high carrier mobility (low band effective mass) and high thermopower (high DOS effective mass).

### 3.3 Predicted thermoelectric performance

Fig. 7 presents the predicted n-type thermoelectric performance of the 13 stable ABX<sub>4</sub> phases; the 7 newly predicted ABX<sub>4</sub> phases are labeled. The computed intrinsic electron mobility ( $\mu_e$ ) is plotted as a function of the lattice thermal conductivity  $(\kappa_{\rm I})$ , with the color scheme representing the CB degeneracy  $(N_{\rm b,CB})$  in Fig. 7(a) and the DOS effective mass  $(m_{DOS,CB}^*)$  in Fig. 7(b). The size of the markers scales with n-type  $\beta$ . The  $\beta$  for n-type PbTe is shown for reference in Fig. 7(a). In general, we find that the 13 ABX<sub>4</sub> phases exhibit low  $\kappa_{\rm L}$  (<1.5 W mK<sup>-1</sup>) and high  $\mu_{\rm e}$  (75 to 150 cm<sup>2</sup> V<sup>-1</sup> s<sup>-1</sup>), which indicates that ABX<sub>4</sub> Zintl phases are promising n-type materials for thermoelectrics.

The predicted transport properties and TE performance assessment are summarized in Table 1, sorted in the descending order of their n-type  $\beta$  values. All 13 compounds in Table 1 have relatively high n-type TE performance – larger  $\beta$  than PbTe, when optimally doped. NaGaSb4 and NaAlSb4 stand out as the most promising candidates with the highest normalized  $\beta/\beta_{PbTe}$ of 4.8 and 4.5, respectively. The high predicted n-type TE performance of NaGaSb4 and NaAlSb4 can be primarily attributed to their high conduction band degeneracy of 7 and 6, respectively, which is larger than that of other ABX4 phases  $(N_{\rm b,CB}=2)$ . Coupled with moderately low CB effective mass (0.072 for NaAlSb4 and 0.090 for NaGaSb4), the high band degeneracy leads to high DOS effective mass, as shown in Fig. 7(b). The full assessment of the transport properties and TE performance of the 13 ABX<sub>4</sub> phases is available in the ESI.† The data will be also made available on our thermoelectrics-focused database, **TEDesignLab** open-access (http:// www.tedesignlab.org).33

## Defect chemistry of ABX<sub>4</sub> Zintl phases

Although  $\beta$  serves to screen candidate TE materials, the successful prediction relies on a key assumption - the material must be optimally doped with electrons or holes, depending on n- or p-type TE. Materials with high  $\beta$  may be insulators or suffer from doping asymmetry. In such cases, the predicted TE performance cannot be realized. Therefore, we perform firstprinciples defect calculations to assess the dopability of the newly predicted candidate ABX4 phases.

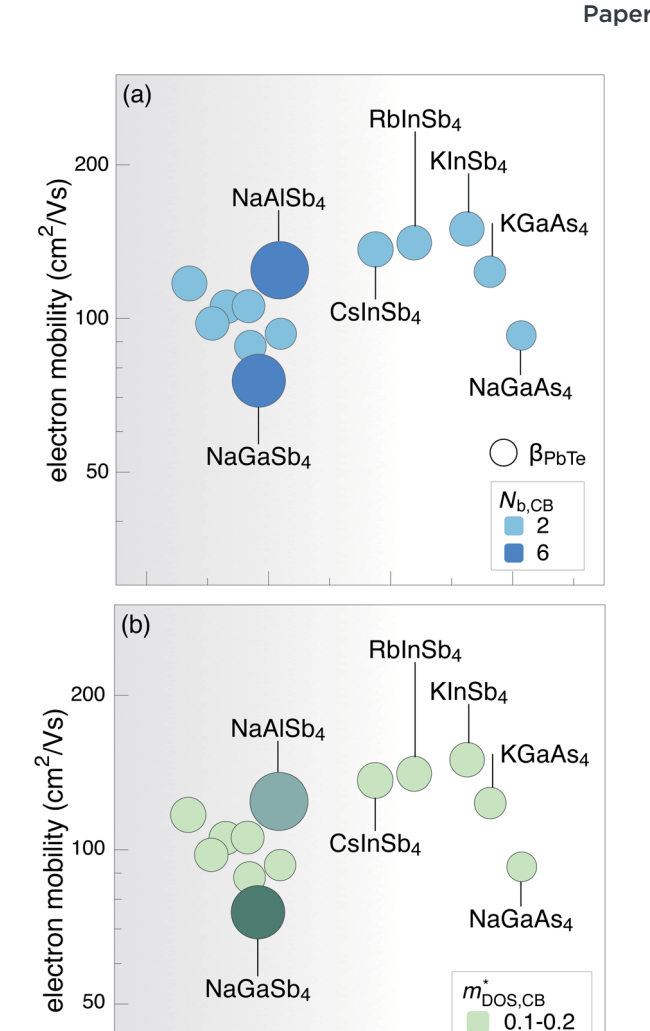


Fig. 7 Calculated n-type quality factor  $(\beta)$  plotted as a function of the computed room-temperature electron mobility and lattice thermal conductivity. The marker size scales with the value of  $\beta$ . For reference, the marker size corresponding to the  $\beta$  value of PbTe (15) is shown as a legend. The color scheme in (a) denotes the conduction band degeneracy ( $N_{b,CB}$ ) while in (b) the conduction band density-of-states (DOS) effective mass  $(m_{\text{DOS,CB}}^*)$ . The 7 newly predicted stable ABX<sub>4</sub> Zintl phases are labeled.

1.2

lattice thermal conductivity (W/mK)

1.0

0.8

For defect calculations, we select the top three candidate materials (NaAlSb<sub>4</sub>, NaGaSb<sub>4</sub>, and CsInSb<sub>4</sub>) from Table 1 and assess their n-type dopability. These three candidate materials are composed of relatively earth-abundant and non-toxic elements. We assess the n-type dopability under the most alkali-rich conditions within the phase stability region because the formation of the dominant electron-compensating, acceptor alkali vacancies is suppressed under those conditions. The acceptor cation vacancies, colloquially referred to as "killer defects", compensate electron doping by extrinsic dopants. The existence of cation vacancies with low formation energy is the primary cause of self p-type doping or difficulty in n-type doping

in Zintl phases. 18 As such, Zintl phases where cation vacancies have high formation energies are considered n-type dopable. While n-type dopable Zintl phases are rare, we show here that our targeted search has enabled us to "design" as-yet-unknown Zintl phases with the desired doping characteristics as well as thermoelectric performance.

The calculated formation energies of native point defects (vacancies, anti-site defects and interstitials) in NaAlSb<sub>4</sub>, NaGaSb<sub>4</sub> and CsInSb<sub>4</sub> under alkali-rich conditions are shown in Fig. 8. The n-type dopability can be quantitatively assessed by  $\Delta E_{\rm don}$  – which is the energy "window" at the CBM formed by the lowest-energy acceptor defects. If  $\Delta E_{\rm don}$  is large, then there is a better chance for n-type doping because of the limited electron compensation by the acceptor defects. The  $\Delta E_{\mathrm{don}}$  values for NaAlSb<sub>4</sub>, NaGaSb<sub>4</sub> and CsInSb<sub>4</sub> are large and positive - 0.34 eV, 0.30 eV and 0.47 eV under alkali-poor growth conditions, respectively. In contrast,  $\Delta E_{\rm don}$  in well-known Zintl phases are typically negative. For example,  $\Delta E_{\rm don}$  for Ca<sub>5</sub>Al<sub>2</sub>Sb<sub>6</sub> is -0.1 eV.<sup>18</sup>

NaAlSb<sub>4</sub>. The formation energies  $(\Delta E_{D,q})$  of native point defects under the most Na-rich growth conditions are shown in Fig. 8(a). The lowest-energy acceptor defects are sodium vacancies V<sub>Na</sub> and donors are anti-site defects Sb<sub>Al</sub> and Na interstitials Nai. The equilibrium Fermi energy is usually in the vicinity of the intersection between the lowest-energy defects. In this case, the equilibrium Fermi energy lies around the mid-gap (marked by the dotted line in Fig. 8). The predicted hole concentrations for undoped NaAlSb<sub>4</sub> is  $6.5 \times 10^{17}$  cm<sup>-3</sup> at 800 K. However, what is more important is the high formation

energy of acceptor Na vacancies, which creates a large n-type dopability window  $\Delta E_{\text{don}}$  of 0.34 eV. Under the most Na-poor conditions (Fig. S3(a) $\dagger$ ), the formation energy of  $V_{Na}$  is slightly lower and their concentration higher, when compared to the most Na-rich conditions. Therefore, NaAlSb<sub>4</sub> is n-type dopable with high predicted n-type TE performance.

NaGaSb<sub>4</sub>. The native defect energetics of NaGaSb<sub>4</sub> are similar to those of NaAlSb<sub>4</sub> (Fig. 8(b)). The defect energetics under the most Na-poor conditions are shown in Fig. S3(b) in the ESI.† The predominant native defects are  $Sb_{Ga}$ ,  $Na_i$  and  $V_{Na}$ . The relatively high  $\Delta E_{\mathrm{D},q}$  for  $V_{\mathrm{Na}}$  creates an n-type dopability window of 0.30 eV. The smaller  $\Delta E_{\text{don}}$  can be attributed to the slightly wider band gap of NaGaSb<sub>4</sub> (0.374 eV) compared to NaAlSb<sub>4</sub> (0.357 eV). The equilibrium Fermi energy in undoped NaGaSb<sub>4</sub> under the most Na-rich conditions is closer to the valence band maximum, with an estimated free hole concentration of  $9.4 \times 10^{17} \text{ cm}^{-3}$  at 800 K synthesis temperature.

CsInSb<sub>4</sub>. CsInSb<sub>4</sub> has a wider band gap (0.794 eV) than NaAlSb4 and NaGaSb4 due to the higher electronegativity difference between Cs and In. The native defect energetics of CsInSb<sub>4</sub> under the most Cs-rich growth conditions are shown in Fig. 8(c). The alkali vacancies V<sub>Cs</sub> have even higher formation energy than V<sub>Na</sub> in NaAlSb<sub>4</sub> and NaGaSb<sub>4</sub>. Consequently, the ntype dopability window ( $\Delta E_{\text{don}}$ ) of 0.47 eV is quite large. Thus, CsInSb<sub>4</sub> is likely more n-type dopable than NaAlSb<sub>4</sub> or NaGaSb<sub>4</sub>. In contrast with NaAlSb4 and NaGaSb4, p-type dopability of CsInSb<sub>4</sub> is limited by the low energy donor Sb<sub>In</sub> anti-site defects under the most Cs-rich growth conditions. Undoped CsInSb₄ is

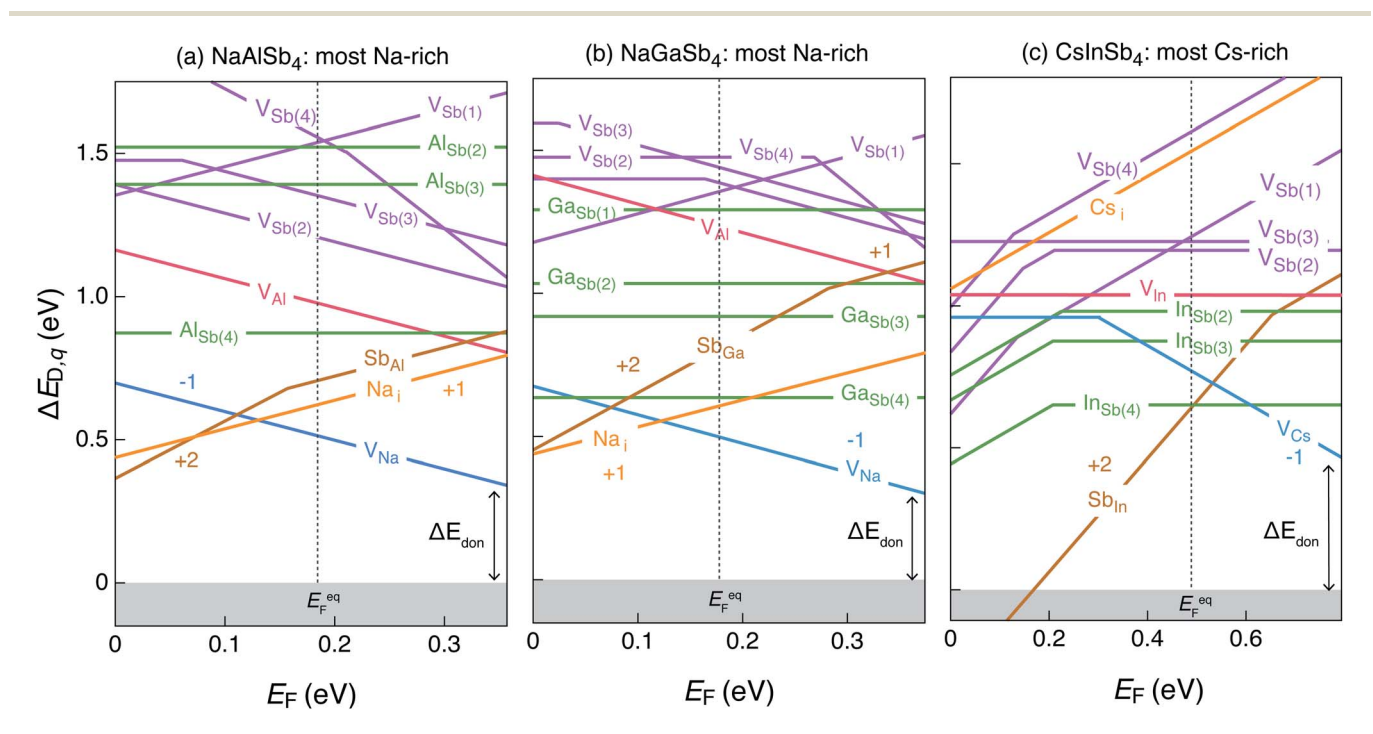


Fig. 8 Formation energies of native defects ( $\Delta E_{D,g}$ ) as a function of Fermi energy ( $E_F$ ) for (a) NaAlSb<sub>4</sub> (under the most Na-rich conditions), (b) NaGaSb<sub>4</sub> (under the most Na-rich conditions), and (c) CsInSb<sub>4</sub> (under the most Cs-rich conditions). E<sub>F</sub> is referenced to the valence band maximum and  $E_F$  values can range from 0 to the band gap. The slope of the line is equal to the charge state of the defect. The lowest energy acceptors are alkali vacancies (in blue), which restrict  $\Delta E_{don}$  to 0.34, 0.30 and 0.47 for NaAlSb<sub>4</sub>, NaGaSb<sub>4</sub> and CsInSb<sub>4</sub> respectively.  $\Delta E_{don}$ represents the n-type dopability window for extrinsic dopants. The equilibrium  $E_F$  (dashed vertical lines) is calculated at 800 K.

predicted to be lightly n-type with a free electron concentration of  $3.0 \times 10^{16}$  cm<sup>-3</sup>, assuming synthesis at 800 K. In summary, we find the three newly predicted ABX4 Zintl phases, namely, NaAlSb<sub>4</sub>, NaGaSb<sub>4</sub> and CsInSb<sub>4</sub>, to be n-type dopable. Among these three candidates, CsInSb<sub>4</sub> has the largest n-type dopability window of 0.47 eV followed by NaAlSb<sub>4</sub> (0.34 eV) and NaGaSb<sub>4</sub> (0.30 eV). Future work will explore possible extrinsic donor dopants to achieve optimal n-type doping that maximize the thermoelectric performance. In a prior study,12 we found Ba to be an effective n-type dopant for KGaSb4, with free electron concentrations exceeding  $1 \times 10^{19} \text{ cm}^{-3}$ . This suggests that it may be possible to find suitable n-type dopants for the candidate phases, NaAlSb4, NaGaSb4 and CsInSb4. The demonstration of n-type dopability of the new ABX4 Zintl phases, constructed by chemical replacements, provides further confidence in the "doping by design" strategy undertaken in this study.

## 4 Conclusions

In this work, we utilize a new route to "designing" materials with desired doping and functional characteristics. We hypothesize that the doping properties and functional performance of the prototype structure are translated to new compounds created by chemical replacements, and we demonstrate this design strategy by discovering new n-type dopable ABX4 Zintl phases. We perform first-principles calculations to explore 36 hypothetical ABX4 Zintl phases in the  $KGaSb_4$  structure, where A = Na, K, Cs, Rb, B = Al, Ga, In, and X= Sb, As, Bi, and assess their stability and n-type TE performance. We find 13 stable ABX<sub>4</sub> phases, including 6 known and 7 as-yet-unreported ABX4 phases. Among the newly discovered phases, we consider the top candidates (NaAlSb4, NaGaSb4, and CsInSb<sub>4</sub>) with the highest predicted n-type TE performance, and show that they are n-type dopable. Therefore, we have demonstrated that the design strategy to discover new n-type Zintl phases is to perform chemical replacements in prototype structures that are known to be n-type dopable. This exciting materials design approach offers an exciting route to discovering new compounds with desired doping and functional performance that may have applications beyond thermoelectrics.

## Conflicts of interest

There are no conflicts to declare.

## Acknowledgements

JQ is funded by the NSF DIGI-MAT program, grant no. 1922758. PG and VS acknowledge support from the NSF DMR program, grant no. 1729594. EE acknowledges support from the NSF DMR program, grant no. 1729149. The research was performed using computational resources sponsored by the Department of Energy's Office of Energy Efficiency and Renewable Energy and located at the NREL.

## References

- 1 J. He and T. M. Tritt, Science, 2017, 357, 1.
- 2 P. Gorai, V. Stevanović and E. S. Toberer, *Nat. Rev. Mater.*, 2017, 2, 1-16.
- 3 H. Mizoguchi, T. Kamiya, S. Matsuishi and H. Hosono, *Nat. Commun.*, 2011, 2, 1–5.
- 4 H. Kawazoe, M. Yasukawa, H. Hyodo, M. Kurita, H. Yanagi and H. Hosono, *Nature*, 1997, 389, 939–942.
- 5 M. Chan, S. Lai, M. Fung, C. Lee and S. Lee, *Appl. Phys. Lett.*, 2007, **90**, 023504.
- 6 M. Y. Chan, S. L. Lai, M. K. Fung, C. S. Lee and S. T. Lee, *Appl. Phys. Lett.*, 2007, **90**, 023504.
- 7 A. Janotti and C. G. Van de Walle, *Phys. Rev. B: Condens. Matter Mater. Phys.*, 2007, **76**, 165202.
- 8 P. Gorai, P. Parilla, E. S. Toberer and V. Stevanovic, *Chem. Mater.*, 2015, 27, 6213.
- 9 L. Bjerg, G. K. H. Madsen and B. B. Iversen, *Chem. Mater.*, 2012, **24**, 2111–2116.
- 10 P. J. Shaver and J. Blair, Phys. Rev., 1966, 141, 649-663.
- 11 B. R. Ortiz, P. Gorai, L. Krishna, R. Mow, A. Lopez, R. McKinney, V. Stevanović and E. S. Toberer, *J. Mater. Chem. A*, 2017, 5, 4036–4046.
- 12 B. R. Ortiz, P. Gorai, V. Stevanovic and E. S. Toberer, *Chem. Mater.*, 2017, 29, 4523–4534.
- 13 B. R. Ortiz, P. Gorai, T. Braden, E. A. Bensen, S. D. Wilson, V. Stevanović and E. S. Toberer, ACS Appl. Energy Mater., 2020, 3, 2182–2191.
- 14 A. Balvanz, S. Baranets and S. Bobev, *J. Solid State Chem.*, 2020, 121476, accepted.
- 15 S. R. Brown, S. M. Kauzlarich, F. Gascoin and G. J. Snyder, *Chem. Mater.*, 2006, **18**, 1873–1877.
- 16 R. Marchand and W. Jeitschko, J. Solid State Chem., 1978, 24, 351–357.
- 17 E. S. Toberer, A. Zevalkink, N. Crisosto and G. J. Snyder, *Adv. Funct. Mater.*, 2010, 20, 4375–4380.
- 18 P. Gorai, A. Goyal, E. S. Toberer and V. Stevanović, *J. Mater. Chem. A*, 2019, 7, 19385–19395.
- 19 P. Gorai, A. M. Ganose, A. Faghaninia, A. Jain and V. Stevanovic, *Mater. Horiz.*, 2020, 7, 1809–1818.
- 20 R. Gautier, X. Zhang, L. Hu, L. Yu, Y. Lin, T. O. Sunde, D. Chon, K. R. Poeppelmeier and A. Zunger, *Nat. Chem.*, 2015, 7, 308.
- 21 X. Zhang, L. Yu, A. Zakutayev and A. Zunger, *Adv. Funct. Mater.*, 2012, **22**, 1425.
- 22 B. Meredig, A. Agrawal, S. Kirklin, J. E. Saal, J. W. Doak, A. Thompson, K. Zhang, A. Choudhary and C. Wolverton, Phys. Rev. B: Condens. Matter Mater. Phys., 2014, 89, 094104.
- 23 C. E. Wilmer, M. Leaf, C. Y. Lee, O. K. Farha, B. G. Hauser, J. T. Hupp and R. Q. Snurr, *Nat. Chem.*, 2012, 4, 83.
- 24 Y. Hinuma, T. Hatakeyama, Y. Kumagai, L. A. Burton, H. Sato, Y. Muraba, S. Iimura, H. Hiramatsu, I. Tanaka, H. Hosono, *et al.*, *Nat. Commun.*, 2016, 7, 1.
- 25 M. R. Filip and F. Giustino, J. Phys. Chem. C, 2016, 120, 166.
- 26 A. Belsky, M. Hellenbrandt, V. L. Karen and P. Luksch, *Acta Crystallogr., Sect. B: Struct. Sci.*, 2002, **58**, 364.

- 27 G. Kresse and J. Furthmüller, Phys. Rev. B: Condens. Matter Mater. Phys., 1996, 54, 11169-11186.
- 28 J. P. Perdew, K. Burke and M. Ernzerhof, Phys. Rev. Lett., 1996, 77, 3865-3868.
- 29 P. E. Blöchl, Phys. Rev. B: Condens. Matter Mater. Phys., 1994, 50, 17953-17979.
- 30 J. Yan, P. Gorai, B. Ortiz, S. Miller, S. A. Barnett, T. Mason, V. Stevanović and E. S. Toberer, Energy Environ. Sci., 2015, 8, 983-994.
- 31 S. A. Miller, P. Gorai, B. R. Ortiz, A. Goyal, D. Gao, S. A. Barnett, T. O. Mason, G. J. Snyder, Q. Lv, V. Stevanović and E. S. Toberer, Chem. Mater., 2017, 29, 2494-2501.
- 32 F. Birch, J. Geophys. Res., 1952, 57, 227-286.
- 33 P. Gorai, D. Gao, B. Ortiz, S. Miller, S. A. Barnett, T. Mason, Q. Lv, V. Stevanovic and E. S. Toberer, Comput. Mater. Sci., 2016, 112, 368.
- 34 S. Ohno, K. Imasato, S. Anand, H. Tamaki, S. D. Kang, P. Gorai, H. K. Sato, E. S. Toberer, T. Kanno and G. J. Snyder, Joule, 2017, 2, 141.

- 35 P. Gorai, E. S. Toberer and V. Stevanovic, J. Appl. Phys., 2019, 125, 025105.
- 36 G. Hautier, S. P. Ong, A. Jain, C. J. Moore and G. Ceder, Phys. Rev. B: Condens. Matter Mater. Phys., 2012, 85, 155208.
- 37 V. Stevanović, S. Lany, X. Zhang and A. Zunger, Phys. Rev. B: Condens. Matter Mater. Phys., 2012, 85, 115104.
- 38 A. Togo, F. Oba and I. Tanaka, Phys. Rev. B: Condens. Matter Mater. Phys., 2008, 78, 134106.
- 39 A. Togo and I. Tanaka, Scr. Mater., 2015, 108, 1-5.
- 40 S. Lany and A. Zunger, Phys. Rev. B: Condens. Matter Mater. Phys., 2008, 78, 235104.
- 41 H. Peng, D. O. Scanlon, V. Stevanovic, J. Vidal, G. W. Watson and S. Lany, Phys. Rev. B: Condens. Matter Mater. Phys., 2013, 88, 115201.
- 42 A. Goyal, P. Gorai, H. Peng, S. Lany and V. Stevanovic, Comput. Mater. Sci., 2017, 130, 1.
- 43 W. Li, J. Carrete, G. K. H. Madsen and N. Mingo, Phys. Rev. B, 2016, 93, 205203.